

## **Attenuation correction for a combined 3D PET/CT scanner**

P. E. Kinahan, D. W. Townsend, T. Beyer, and D. Sashin

*Department of Radiology, University of Pittsburgh, 200 Lothrop Street, Pittsburgh, PA 15213*

In this work we demonstrate the proof of principle of CT-based attenuation correction of 3D Positron Emission Tomography (PET) data by using scans of bone and soft tissue equivalent phantoms and scans of humans. This method of attenuation correction is intended for use in a single scanner that combines volume-imaging (3D) PET with X-ray Computed Tomography (CT) for the purpose of providing accurately registered anatomical localization of structures seen in the PET image. The goal of this work is to determine if we can perform attenuation correction of the PET emission data using accurately aligned CT attenuation information. We discuss possible methods of calculating the PET attenuation map at 511 keV based on CT transmission information acquired from 40 keV through 140 keV. Data were acquired on separate CT and PET scanners and were aligned using standard image registration procedures. Results are presented on three of the attenuation calculation methods: segmentation, scaling, and our proposed hybrid segmentation/scaling method. The results are compared with those using the standard 3D PET attenuation correction method as a gold standard. We demonstrate the efficacy of our proposed hybrid method for converting the CT attenuation map from an effective CT photon energy of 70 keV to the PET photon energy of 511 keV. We conclude that using CT information is a feasible way to obtain attenuation correction factors for 3D PET.

Key words: dual modality, PET and CT, attenuation correction

## I. INTRODUCTION

While still in an early phase, the role of PET imaging in oncology research and patient care is clearly growing <sup>1</sup>. The increased uptake of [<sup>18</sup>F]fluorodeoxyglucose, or FDG, by neoplasms can significantly influence patient management and predict survival probability, particularly for breast, lung, and colorectal cancers <sup>2</sup>.

In regions such as the thorax and abdomen, the demonstration of increased FDG uptake is limited in value without an unambiguous localization of tracer uptake to a specific structure, for example, a tumor seen on a corresponding CT image. Post-hoc PET-CT alignment, however, is difficult due to shifting of the position of organs, which can occur without patient motion and may even depend upon the relative curvature of the patient beds of the separate scanners.

To address this problem, a single tomograph with the unique capability of acquiring both functional (PET) and anatomical (CT) images is being built as a collaboration between the University of Pittsburgh and Siemens/CTI, and funded in part by the National Cancer Institute. The purpose of the project is to construct a scanner for oncology imaging that provides accurately aligned functional and anatomical images.

The PET/CT scanner design is based on a third-generation rotating fan-beam CT scanner, the Siemens Somatom AR.SP. The AR.SP can operate in a rapid helical scanning mode and has an in-plane resolution of better than 1 mm. The PET component is based on the rotating ECAT ART<sup>1</sup> (Advanced Rotating Tomograph) scanner manufactured by Siemens/CTI. The ART scanner has a spatial resolution of 6 mm in all directions, and for the NEMA-PET phantom (described below) has a scatter-subtracted sensitivity of approximately 300 kcps/ $\mu$ Ci/ml <sup>3</sup>. Unlike most commercial scanners the ART scanner operates without retractable shielding rings, or septa, and is thus a volume, or 3D, imaging system with a 16.2 cm axial field-of-view. The 3D imaging of the ART scanner also results in a scatter fraction (scatter/total) of 36% as compared to approximately 12% for PET scanners imaging in 2D mode with the septa extended into the field of view. The increased scatter fraction, however, is adequately removed from the image by a model-based scatter correction procedure <sup>4</sup>.

---

<sup>1</sup> CTI PET Systems Inc. 810 Innovation Drive, Knoxville, TN 37932-2571

For the combined PET/CT scanner, the two bismuth germanate (BGO) PET detector arrays from the ART scanner will be mounted on the rotating support of the AR.SP CT system, as is conceptually illustrated in figure 1. Data will be acquired during continuous rotation of the gantry and read out through an optical slip-ring system. The PET and CT data will not be acquired simultaneously, however, and the two imaging functions will operate independently. The PET detector array will collect emission data in 3D mode over a 16.2 cm axial field-of-view, whereas CT volumes corresponding to the PET field-of-view will be obtained by an appropriate patient bed motion during a separate spiral scan.

The effect of photon attenuation in PET imaging is usually directly measured in coincident transmission mode with  $^{68}\text{Ge}/^{68}\text{Ga}$  sources of 511 keV annihilation photons. It is undesirable to acquire the transmission data in 3D mode, as the typical 40-70 MBq activity of rod sources results in excessive dead-time of the near-side detector. To reduce dead-time effects for PET scanners that operate in 3D mode only, such as the ART, low activity transmission rod sources are used. This use of low activity sources significantly increases statistical noise effects<sup>2</sup>.

An alternative approach that is possible with the PET/CT scanner is the use of CT-based attenuation correction and this paper evaluates the efficacy of such an approach. The potential advantages of using CT transmission scans for attenuation correction are:

- CT transmission scans that are acquired after the injection of the PET tracer will not suffer from contamination by 511 keV photons emitted from the PET tracer, due to the much higher flux of the CT photons. Post-injection transmission scans are desirable in clinical settings as they increase patient comfort and scanner throughput.
- The CT data will have much lower statistical noise than a standard PET transmission scan, thus reducing statistical noise in the final attenuation-corrected PET emission image, especially for whole-body PET imaging. In addition, the shorter times required for the collection of the CT transmission data means longer times for the acquisition of the PET emission scan, thus lowering statistical noise even further for a constant *total* (emission+transmission) scan duration.

---

<sup>2</sup> An alternative method of transmission imaging developed for 3D-only PET scanners has been to use a  $^{137}\text{Cs}$  point source of single 662 keV gamma-ray photons <sup>5</sup>.

- It will no longer be necessary to include the standard PET transmission sources, thus eliminating the cost both of including these components and the periodic replacement of decayed radioactive transmission sources.

Another potential advantage of a PET/CT scanner is the incorporation of CT data directly into the image reconstruction process. This can be done with a maximum a posteriori image reconstruction algorithm <sup>6</sup>, although the topic is beyond the scope of the work reported here. In this work we do not address issues of breath-holding during CT scans, or the use of contrast agents. Investigation of these issues will have to await operational studies from the PET/CT scanner.

For all the methods described here, the CT attenuation image is used as a basis for estimating the PET attenuation image, replacing the usual attenuation image reconstructed from a PET transmission scan. This is illustrated in figure 2, which also shows the differences between the standard PET attenuation correction methods <sup>7</sup> and the CT-based methods described here. Since the attenuation coefficients,  $\mu(\mathbf{x}, E)$ , are energy-dependent, coefficients measured at CT energies must be converted to the appropriate values at 511 keV if they are to be used to correct PET emission data. Once  $\mu(\mathbf{x}, E)$  at the correct energy is obtained, the attenuation correction factor (ACF) for an individual sinogram element is calculated by numerically integrating  $\exp(\int \mu(\mathbf{x}, E) d\mathbf{x})$  along the line-of-response corresponding to the emission sinogram element.

PET uses mono-energetic 511 keV annihilation photons, whereas the X-ray source in CT emits photons with a broad energy spectrum from 40 keV to 140 keV <sup>8</sup>. This presents two potential difficulties with scaling CT attenuation factors for use with PET data. The first problem is the large difference in photon energies between PET and CT, while the second is the difference between the monochromatic and wide-band energy spectra. For energies below the pair-production threshold of 1022 keV, attenuation is a combination of both Compton scattering and photoelectric absorption. At 511 keV the contribution of photoelectric absorption is essentially negligible for all biological materials. In the CT energy range, however, the dominant effect in bone is photoelectric absorption. This is indicated in Table I, which lists mass attenuation coefficients <sup>9</sup> for some materials of interest.

A method that solves both of the problems of scaling CT attenuation factors for use with PET data is to acquire the CT image at two different energies and use these data to extract the individual photoelectric and Compton contributions of the attenuation <sup>8</sup>. The different contributions can then

be scaled separately in energy and combined to form a mono-energetic attenuation map at any energy below 1022 keV. This approach was used to form a mono-energetic attenuation map at 140 keV by Hasegawa et al. for a prototype SPECT/CT detector block<sup>10</sup>. A potential disadvantage of the dual-energy CT method is that it may contribute additional patient radiation dose. As shown below, however, simpler methods provide acceptable results, so we do not consider this method further.

## II. METHODS

For all studies, the PET data were acquired with a Siemens/CTI ECAT 951R/31 PET tomograph, which has retractable septa and can thus operate in 2D or 3D mode. The ECAT 951R/31 scanner has ~6 mm transaxial resolution, 3.4 mm axial slice spacing and a 10.8 cm axial field of view. The PET images were reconstructed with the 3DRP algorithm<sup>11</sup> implemented on a BC-1 processor<sup>3</sup>. The axial FOV was divided into 31 slices, each 3.4 mm thick. CT scans were acquired with a General Electric 9800 series CT scanner, with 1 mm transaxial resolution and with plane spacing and thickness set to 5 mm. The conventional CT scans were acquired with standard torso imaging parameters of 120 kVp, 140 mA, and with 2 s scan time per slice.

### A. CT-Based Attenuation Correction Methods

We evaluated three methods to obtain 511 keV attenuation correction factors from a CT scan:

**Scaling.** The scaling approach estimates the attenuation image at 511 keV by multiplying the CT image by the ratio of attenuation coefficients of water at CT and PET energies. A single 'effective' energy is chosen to represent the CT spectrum, typically in the range of 50 to 80 keV. LaCroix et al.<sup>12</sup> performed simulation studies to investigate different techniques for scaling the attenuation coefficients from CT energies to 140 keV for SPECT. They found that while linear scaling leads to proper attenuation coefficients when the major contribution to  $\mu(\mathbf{x}, E)$  comes from Compton interactions, it is, however, a poor approximation when photoelectric contributions dominate, as they do at lower CT energies. The error is especially large for materials with higher atomic  $Z$  values, such as bone, which contains a relatively large percentage of calcium, and so has a significantly higher photoelectric fraction than water in the range of CT energies. Table I shows measured values for the mass attenuation coefficient at both 80 keV and 511 keV. Note the 3%

---

<sup>3</sup> Byars Consulting Inc. PO Box 6292, Oak Ridge, TN 37831

difference between the values for soft tissue and bone at 511 keV, compared with a 13% difference at CT photon energies.

**Segmentation.** This method forms the attenuation image at 511 keV by segmenting the reconstructed CT image into different tissue types. The CT image values for each tissue type are then replaced with the appropriate attenuation coefficients at 511 keV. Typical choices for tissue types are soft tissue, bone, and lung. A significant problem, however, is that some soft tissue regions will have continuously-varying densities that may not be accurately represented by a discrete set of segmented values, such as, for example, the lungs, where the density varies by as much as 30%<sup>13</sup>.

**Hybrid: Segmentation and Scaling.** The hybrid method that we proposed is based on a combination of the scaling and segmentation methods. The attenuation image at 511 keV is estimated by first using a threshold to separate out the bone component of the CT image, and then using separate scaling factors for the bone and non-bone component. We have shown<sup>14</sup> that the scaling, segmentation and hybrid methods perform well for 2D and 3D CT-based attenuation corrected reconstructions of PET data for the NEMA-PET phantom<sup>4</sup><sup>15</sup>, which is composed of air, water, and Teflon cylinders. This method has also been applied for CT-based attenuation correction of SPECT data from tandem SPECT-CT scanners<sup>16</sup>. This approach relies on the ratio of the attenuation coefficient at any two photon energies being the same, which is true for most materials except bone. The ratios of the mass attenuation coefficient at 70 keV to that at 511 keV for some important substances are given in table II. Note that the ratio differs for elements such as calcium and phosphorous that have a high percentage abundance in bone. Figure 3 shows the mass attenuation coefficient for air, water, muscle and bone as a function of photon energy. The similarities of the values for air, water and muscle indicate that they scale roughly with electron density, due to the dominance of Compton scattering. For energies in the CT range, however the value for bone is higher due to a larger photoelectric fraction caused by the high-Z materials, in particular the ~14% calcium content<sup>9</sup>.

## B. Phantom Studies

These studies were performed for the hybrid method with the NEMA-PET phantom (20 cm diameter and height) where the standard Teflon and water-filled cylinders were replaced with

---

<sup>4</sup> Data Spectrum Inc. PO Box 16115, Chapel Hill, NC USA 27516-6115

cylinders (5 cm diameter) composed of cortical and spongiosa bone equivalent plastic<sup>5</sup> as shown in figure 4. The bone equivalent plastics match within 1% the photon absorption characteristics of spongiosa and cortical bone over the energy range of 10 keV to 100 MeV<sup>17</sup>.

For each phantom study, three scans of the phantom were performed,

- (1) a 15 min 2D PET transmission scan with  $\sim 10^8$  counts collected,
- (2) a 15 min 3D PET emission scan with  $\sim 20$  MBq in the main cylinder and  $\sim 10^8$  events collected,
- (3) a CT scan of the same section of the phantom.

For the 3D PET emission scan, both upper- and lower-energy sinograms were collected and scatter correction was performed with the dual-energy window method<sup>18</sup> prior to attenuation correction. Note that the PET transmission scan was chosen to be 15 min since increasing the duration of transmission scans beyond 15 min does not change the noise of the attenuation corrected *emission* images. The PET transmission scan was processed using the standard procedure for Siemens/CTI scanners<sup>7</sup> where the ACFs are calculated as  $\log[(\text{smoothed blank scan})/(\text{smoothed transmission scan})]$  and the blank scan is a transmission scan performed without the patient.

The CT image was visually aligned to the PET attenuation image by first using a manual image registration procedure, and then with the automated image registration (AIR) algorithm<sup>19</sup> as a consistency check. The alignment of the phantom images was judged to be accurate within a few millimeters for both of these methods. During the image alignment, the CT scan was re-sampled into the same spatial dimensions as the PET data.

**Effective CT energy.** Phantom studies were performed to both test the validity of approximating the energy spectrum of CT photons with a single effective energy and to determine the effective energy that results in the least quantitative inaccuracy. The CT attenuation image was transformed to 511 keV using a single effective energy representing the true spectrum of CT energies and using ratios of 1.90 for soft tissues and 2.26 for bone. The effective CT energy used in the calculation of the ACFs was varied from 50 keV to 90 keV in 10 keV steps.

The reconstructed emission images were analyzed by placing 4 cm diameter circular regions of interest (ROIs) over each insert and over the background for each transaxial image plane for the central axial 7 cm of the field of view. From the ROI values for each plane, a mean and standard

---

<sup>5</sup> Radiology Support Devices Inc. 1904 E. Dominguez St. Long Beach, CA USA 90810

deviation were calculated for each material and compared to values from images reconstructed using the standard PET transmission ACFs. The effective energy was chosen to be that for which the ROI values best matched those from the image reconstructed using the standard PET transmission ACFs.

**Comparison of Attenuation Correction Methods.** From the results of the above procedure, an effective energy of 70 keV was chosen for both the scaling method and the hybrid method. To test the different methods, phantom studies similar to those described above were performed with the modified NEMA-PET phantom. The ACFs were calculated by forward projection through the attenuation image obtained from the PET transmission scan and the CT image using the scaling, segmentation, and hybrid methods.

For the scaling method a global attenuation coefficient ratio of 1.90 was used, while for the hybrid method a ratio of 1.90 was used for soft tissues and a ratio of 2.26 was used for bone. The segmentation procedure was based on selecting a threshold of 1200 as the mid-point between histogram peaks for water and spongiosa bone, as shown in figure 5. The CT image values for each tissue type were replaced with reference attenuation coefficients at 511 keV<sup>9</sup>.

The reconstructed emission images were again analyzed using the ROI procedure described above, and values from the CT-based attenuation corrected images were compared to those from reconstructed images corrected with the standard PET transmission scan.

### C. Human Studies

To illustrate some of the issues associated with CT-based attenuation correction with patient data, the scaling, segmentation, and hybrid methods were tested with clinical data. The data were acquired with the same PET tomograph and CT scanners used in the phantom studies. In the PET scan, a liver tumor study, the patient first had a 15 min 2D transmission scan and was then injected with 100 MBq of [<sup>18</sup>F]fluorodeoxyglucose. After a 45 min uptake period, a 10 min 3D emission scan was acquired. The CT scan without contrast agent covered the same axial region.

For the segmentation method, the CT image was histogrammed with the results shown in figure 7. Based on the histogram, a threshold at a CT value of 1300 was chosen. The assigned values for the regions were based on reference values<sup>9</sup>. The image reconstruction procedure was similar to that described above for the phantom studies, with the exception that the data were corrected for

scatter using the convolution-subtraction method <sup>20</sup>, since the human emission data were collected with a single energy window.

### III. RESULTS

#### A. Phantom Studies

**Effective CT energy.** The measured emission image ROI values reconstructed with ACFs generated by the hybrid method for the different effective energies are given in Table IV, where the emission image ROI values generated using the standard PET ACFs is also given for comparison. The ROI values from the CT-based attenuation correction method most closely approached the PET-based values at an effective energy of 70 keV. Differences in ROI values were small, however, and not sensitive to the choice of effective energy in the range of 50 keV to 90 keV. Based on the results shown in Table III, 70 keV was chosen as the effective energy that produced the smallest overall differences from the standard PET values.

**Comparison of Methods.** The unsmoothed reconstructed emission PET images using the ACFs obtained by the different methods are shown in figure 6. The reconstructed activity for each of the inserts should be zero. Note that the activity in the cortical bone-equivalent insert is greatly over-estimated when the correction factors are obtained from CT by the simple scaling method. This is also shown quantitatively in Table IV. This artifact is due to the over-estimation of the true attenuation for the LORs passing through this region of the phantom, which leads to over-compensating for the effect of attenuation in the corresponding emission sinogram elements.

#### B. Human Studies

Errors in aligning the CT and PET attenuation images were considerably more likely with the human data than with the phantom data. Out of 5 different clinical CT-PET attenuation image sets studied, none were correctly aligned by the automatic AIR program, and careful manual adjustment was required. The error of this manual alignment was estimated to be approximately 3 mm.

Figure 7 shows the histogram of the CT image. When compared to the phantom studies (figure 5), the CT image values have greater variations in attenuation coefficients for any given material. For example, there is a much broader spread of attenuation coefficients for cortical bone in the human data than in the phantom data. This is due to the increased heterogeneity in biological

materials as compared to the geometrically simple phantom. For the segmentation method, results did not change significantly with the threshold set anywhere in the range of 1200-1400.

Figures 8(a) and 8(b) show sections through the reconstructed PET and CT transmission images of the liver after manual alignment. The results of comparing the standard PET method with the three CT-based attenuation correction methods are illustrated in figures 8(c-f). Note that in figure 8(b) a hypodense region is visible in the CT image that is not present in the PET attenuation image. This variation leads to a corresponding low uptake region in the reconstructed emission images that used CT-based attenuation correction (figures 8(d-f)). This is discussed in more detail in the next section.

To compare the statistical noise in the reconstructions, a 5 cm diameter ROI was placed over a uniform region of the liver. The mean and pixel standard deviation are presented in Table V. The CT-based methods are similar to those obtained with the PET-based attenuation correction, although the standard deviations of the CT-based results are slightly reduced.

#### IV. DISCUSSION AND CONCLUSIONS

For both the scaling and hybrid methods, the optimal choice of an effective energy is close to 70 keV, as indicated by Table III. This value was then used for all subsequent analyses. This conclusion is based on using the PET-derived attenuation correction results as the reference standard. This is justified as our goal is not to improve on the PET-based results, but rather to show that equivalent results can be obtained with CT-based methods.

With the scaling method, the cortical bone attenuation values are not correctly scaled, as is clearly shown in figure 6 and Table IV. This may not be a significant problem in practice due to the low amount of cortical bone present in most images, as shown by the histogram in figure 7. The segmentation method produced the most accurate results of the CT-based methods. Areas of the body where tissue density gradually changes over a few centimeters, however, such as in the lungs<sup>13</sup>, may result in artifacts as segmentation methods enforce regions of uniform density. An alternative segmentation method developed for PET attenuation images by Xu et al.<sup>21</sup> has proven to be robust even in areas of gradually changing tissue density. This method combines tissue classification and measured values, however, so it cannot be used directly to adjust attenuation coefficients. We prefer the hybrid method as it shows good quantitative agreement with the PET-

based results (Table IV) and also avoids potential problems with the scaling and segmentation methods listed above.

The human studies show little difference between the scaling and hybrid methods (Table V), probably as there is only a 2% to 6% cortical bone component in the abdominal images. An additional confounding factor is that the PET and CT scans were acquired separately, thus possibly causing shifting of internal organs between scans, an effect that can be exacerbated by having patient beds with different shapes. In our example, hypodense regions were visible in the CT image (figure 8(b)) that were not visible in the PET attenuation image (figure 8(a)). This was likely due to either the lower resolution of the PET transmission scan or shifting of internal organs and changes in accumulation of colon and bowel gases. The hypodense regions lead to the appearance of low uptake regions in the emission images reconstructed with CT-based attenuation correction (figures 8(b-d)). These differences emphasize the importance of acquiring transmission and emission scans that are inherently aligned. The acquisitions should also be separated by as little time as possible to avoid the problem of changing internal structure, which can be caused by, for example, the accumulation of colon or bowel gases. The overall similarity of the emission images, however, demonstrates the feasibility of CT-based attenuation correction with human data.

The quantitative values for the liver ROI show that all attenuation correction methods give similar results, although the statistical noise in the CT-based methods is slightly lower than the standard PET method (Table V). This is most likely due to the lower statistical noise in the CT attenuation image. We expect a more significant advantage for whole-body PET scans where statistical noise from the transmission scan is more problematic <sup>14</sup>.

Issues that have not been examined here are the effect of using iodine-based CT contrast agents, determining what is the minimum CT photon flux needed for attenuation correction of the PET data, or issues related to respiratory motion during the PET and CT scans. Investigation of these issues will await operational studies from the PET/CT scanner.

The primary purpose of the PET/CT scanner is to provide automatic and accurate alignment of functional and anatomical images. CT-based attenuation correction has additional potential advantages of post-injection transmission scanning, lower statistical noise from transmission scans, and eliminating the need for orbiting transmission sources. This work demonstrates the feasibility of CT-based attenuation correction for 3D PET data, and in particular the use of the hybrid segmentation/scaling method. It is noteworthy that our difficulty in properly registering the

separately acquired PET and CT images of the abdomen in patients is a clear indication of the major advantage offered by a combined PET/CT scanner.

## **ACKNOWLEDGMENTS**

T. Beyer is supported by a grant from Siemens/CTI. This work is also supported by NIH grants CA65856 and CA74135 from the National Cancer Institute. We thank Christian Michel, Thomas Nichols, and Larry Byars for considerable software support. We would also like to acknowledge Michel Defrise, Claude Nahmias, Matthias Egger, Edward Hoffman, James Colsher, Margaret Daube-Witherspoon, Charles Stearns, Benjamin Tsui, Bruce Hasegawa and Mark Basic for helpful discussions.

## REFERENCES

- <sup>1</sup>L. G. Strauss and P. S. Conti, "The applications of PET in clinical oncology," *Journal of Nuclear Medicine* **32**, 623-648 (1991).
- <sup>2</sup>P. Rigo, P. Paulis, B. J. Kaschten *et al.*, "Oncological applications of positron emission tomography with fluorine-18 flurodeoxyglucose," *European Journal of Nuclear Medicine* **23** (12), 1641-1674 (1996).
- <sup>3</sup>D. L. Bailey, H. Young, P. M. Bloomfield *et al.*, "ECAT ART - A continuously rotating PET camera: Performance characteristics, initial clinical studies and installation considerations in a nuclear medicine department," *European Journal of Nuclear Medicine* **24**, 6-25 (1997).
- <sup>4</sup>Charles C. Watson, Danny F. Newport, and Mike E. Casey, "A single scatter simulation technique for scatter correction in three-dimensional PET," in *Three-dimensional image reconstruction in radiology and nuclear medicine*, edited by Pierre Grangeat and Jean-Louis Amans (Kluwer, Dordrecht, The Netherlands, 1996), Vol. 4, pp. 255-268.
- <sup>5</sup>R. A. de Kemp and C. Nahmias, "Attenuation correction in PET using single photon transmission measurement," *Medical Physics* **21**, 771-778 (1994).
- <sup>6</sup>Richard Leahy and X. Yan, "Incorporation of anatomical MR data for improved functional imaging with PET," presented at the Information Processing in Medical Imaging: 12th International Conference, Wye, UK, 1991 (unpublished).
- <sup>7</sup>D. W. Townsend, A. Geissbühler, M. Defrise *et al.*, "Fully three-dimensional reconstruction for a PET camera with retractable septa," *IEEE Transactions on Medical Imaging* **MI-10**, 505-512 (1991).
- <sup>8</sup>R. E. Alvarez and A. Macovski, "Energy-selective reconstructions in X-ray computerized tomography," *Physics in Medicine and Biology* **21**, 733-744 (1976).
- <sup>9</sup>J. H. Hubbell, Report No. NSRDS-NBS 29, 1969.
- <sup>10</sup>B. H. Hasegawa, T. F. Lang, E. L. Brown *et al.*, "Object specific attenuation correction of SPECT with correlated dual-energy X-ray CT," *IEEE Transactions on Nuclear Science* **NS-40**, 1242-1252 (1993).
- <sup>11</sup>P.E. Kinahan and J.G. Rogers, "Analytic 3D image reconstruction using all detected events," *IEEE Transactions on Nuclear Science* **36**, 964-968 (1989).
- <sup>12</sup>K. J. LaCroix, B. M. W. Tsui, B. H. Hasegawa *et al.*, "Investigation of the use of X-ray CT images for attenuation compensation in SPECT," *IEEE Transactions on Nuclear Science* **NS-41**, 2793-2799 (1994).
- <sup>13</sup>P. J. Robinson and L. Kreel, "Pulmonary tissue attenuation with computed tomography: Comparison of inspiration and expiration scans," *Journal of Computer Assisted Tomography* **3**, 740-748 (1979).

- <sup>14</sup>T. Beyer, P. E. Kinahan, D. W. Townsend *et al.*, “The use of X-ray CT for attenuation correction of PET data,” presented at the IEEE Nuclear Science Symposium and Medical Imaging Conference, Norfolk, VA, 1994 (unpublished).
- <sup>15</sup>J. S. Karp, M. E. Daube-Witherspoon, E. J. Hoffman *et al.*, “Performance standards in positron emission tomography,” *Journal of Nuclear Medicine* **32** (12), 2342-50 (1991).
- <sup>16</sup>S. C. Blankenspoor, X. Wu, J. K. Kalki *et al.*, “Attenuation Correction of SPECT Using X-Ray CT on an Emission-Transmission CT System: Myocardial Perfusion Assessment,” *IEEE Transactions on Nuclear Science* **43** (4), 2263-2274 (1996).
- <sup>17</sup>International Commission on Radiation Units and Measurements, Report No. 44, 1989.
- <sup>18</sup>S. Grootenk, T. J. Spinks, T. Jones *et al.*, “Correction for scatter using a dual energy window technique with a tomograph operating without septa,” presented at the IEEE Nuclear Science Symposium and Medical Imaging Conference, Orlando, FL, 1992 (unpublished).
- <sup>19</sup>R. P. Woods, S. R. Cherry, and J. C. Mazziotta, “Rapid automated algorithm for aligning and reslicing PET images,” *Journal of Computer Assisted Tomography* **16**, 620-633 (1992).
- <sup>20</sup>D. L. Bailey and S. R. Meikle, “A convolution-subtraction scatter correction method for 3D PET,” *Physics in Medicine and Biology* , 412-424 (1994).
- <sup>21</sup>M. Xu, P. D. Cutler, and W. K. Luk, “Adaptive segmented attenuation correction for whole-body PET imaging,” *IEEE Transactions on Nuclear Science* **NS-43**, 331-336 (1996).

**TABLES**

Table I. Mass attenuation coefficients (linear attenuation coefficient / density) in cm<sup>2</sup>/g. Data are from Hubbell <sup>9</sup>.

Material	80 keV			500 keV			Ratio of totals
	photoelec.	Compton	total	photoelec.	Compton	total	80keV:500keV
Air	0.006	0.161	0.167	< 0.001	0.087	0.087	1.92
Water	0.006	0.178	0.184	< 0.001	0.097	0.097	1.90
Muscle	0.006	0.176	0.182	< 0.001	0.096	0.096	1.90
Bone	0.034	0.175	0.209	< 0.001	0.093	0.093	2.26
Teflon	---	---	0.168	---	---	0.087	1.93

Table II. Ratios of attenuation coefficient at 70 keV to that at 511. Calculated from Hubbell <sup>9</sup>.

Material	Ratio 70 keV : 511 keV
nitrogen	1.83
carbon	1.80
oxygen	1.86
air	1.85
water	1.84
calcium	4.02
phosphorous	3.70
bone	2.26

Table III. ROI values (kBq/ml) from reconstructed emission scans using different effective CT energies for attenuation correction factors calculated by the hybrid segmentation/scaling method.

Energy (keV)	Background	Air	Cortical equiv.
PET	$1.26 \pm 0.08$	$0.16 \pm 0.07$	$0.11 \pm 0.01$
50	$1.22 \pm 0.08$	$0.05 \pm 0.07$	<0
60	$1.25 \pm 0.08$	$0.02 \pm 0.07$	<0
70	$1.26 \pm 0.08$	$0.12 \pm 0.07$	$0.08 \pm 0.10$
80	$1.29 \pm 0.08$	<0	$0.16 \pm 0.10$
90	$1.30 \pm 0.08$	<0	$0.24 \pm 0.10$

Table IV. ROI values from reconstructed transmission and emission scans for the different attenuation correction methods. PET = PET attenuation image. CT-Scl = Scaled CT image. CT-Seg = Segmented CT image. CT-Hyb = Hybrid segmented/scaled CT image. The effective energy used for the scaling and hybrid methods was 70 keV. Expected linear attenuation coefficients are from Hubble<sup>9</sup>, while expected emission values are based on cross-calibration with a well-counter.

Method	Background (water)	Air	Cortical equiv.	Spongiosa equiv.
Linear attenuation values (cm <sup>-1</sup> )				
Expected	0.096	0.0001	0.173	0.112
PET	0.098	0.008	0.169	0.113
CT-Scl	0.097	0.007	0.224	0.126
CT-Seg	0.096	0.0001	0.173	0.112
CT-Hyb	0.097	0.007	0.164	0.105
Emission values (kBq/ml)				
Expected	$1.26 \pm 0.13$	0	0	0
PET	$1.26 \pm 0.08$	$0.16 \pm 0.07$	$0.10 \pm 0.01$	$0.05 \pm 0.08$
CT-Scl	$1.35 \pm 0.08$	$-0.08 \pm 0.08$	$1.18 \pm 0.11$	$0.19 \pm 0.08$
CT-Seg	$1.21 \pm 0.07$	$0.0 \pm 0.07$	$0.10 \pm 0.01$	$-0.02 \pm 0.07$
CT-Hyb	$1.26 \pm 0.08$	$0.12 \pm 0.07$	$0.08 \pm 0.01$	$-0.26 \pm 0.08$

Table V. Mean and standard deviation for a 5 cm diameter ROI placed over the liver in figure 8.

Method	mean $\pm$ std. dev. (kBq/ml)
PET	3.7 $\pm$ 0.6
CT-scaled	3.5 $\pm$ 0.3
CT-segmented	3.6 $\pm$ 0.3
CT-hybrid	3.4 $\pm$ 0.3

**FIGURE CAPTIONS**

Figure 1. Illustration of the PET/CT scanner operational principles. The continuous rotation of the detectors allows collection of full projection data sets for the PET and CT subsystems. With no septa, the PET detector arrays are operated in 3D (high-sensitivity) mode, and are mounted forward of the CT system on the same rotating support. Data will be acquired and read out during continuous rotation through optical slip-rings.

Figure 2. Data processing flow chart for 3D attenuation correction and image reconstruction. The data and procedures involving the CT data (dashed box) are those proposed in this paper.

Figure 3. Mass attenuation coefficient for materials of interest as a function of photon energy. Data are from Hubbell <sup>9</sup>.

Figure 4. Schematic of the NEMA-PET phantom with cylindrical inserts.

Figure 5. Histogram of the NEMA-PET CT image. The different materials are identified. The CT values are (Hounsfield units + 1024).

Figure 6. Emission images (ramp-filtered) of the NEMA-PET phantom with attenuation correction using: (a) the PET transmission scan, (b) the CT scan with the scaling method, (c) the CT scan with segmentation method, and (d) the CT scan with the hybrid method.

Figure 7. Histogram of the patient CT image shown in figure 7(b). The CT values are (Hounsfield units + 1024).

Figure 8. Aligned attenuation and emission images of the abdomen of a patient with a hepatocellular carcinoma. Attenuation images: (a) PET and (b) CT. Emission images with attenuation correction done using: (c) standard PET method, (d) scaled CT image, (e) segmented CT image, and (f) hybrid segmented/scaled CT image. The arrows indicate the position of the tumor.

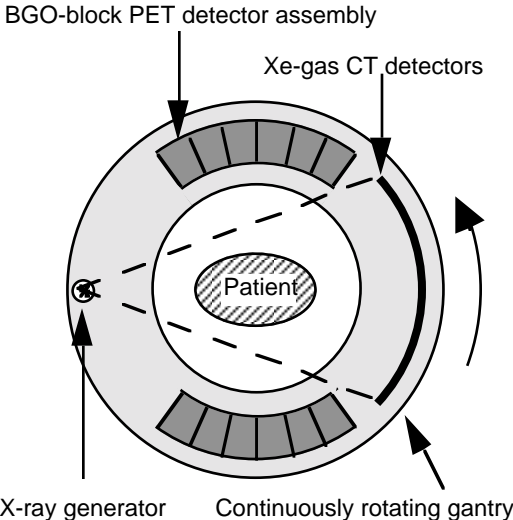


Figure 1

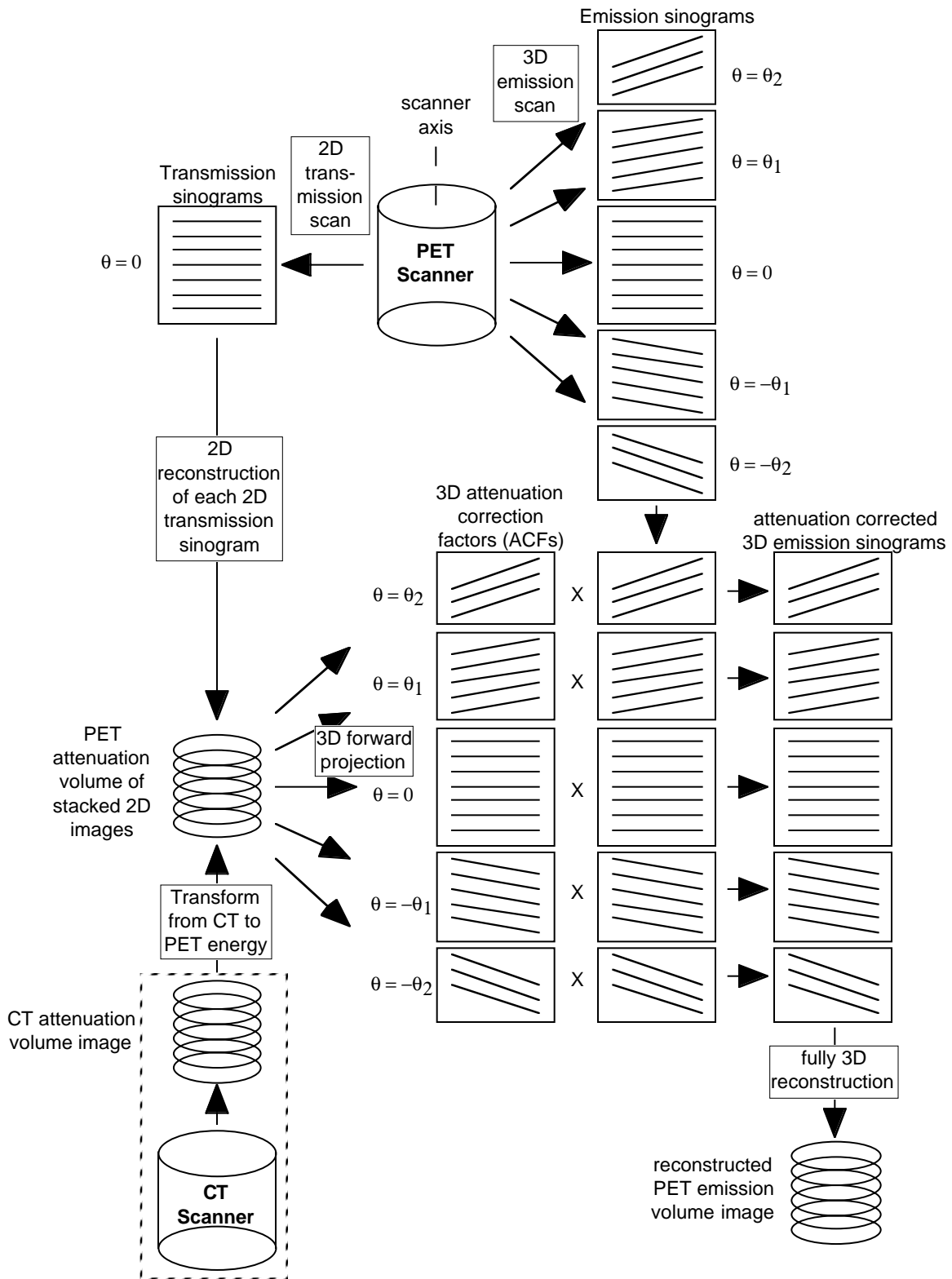


Figure 2

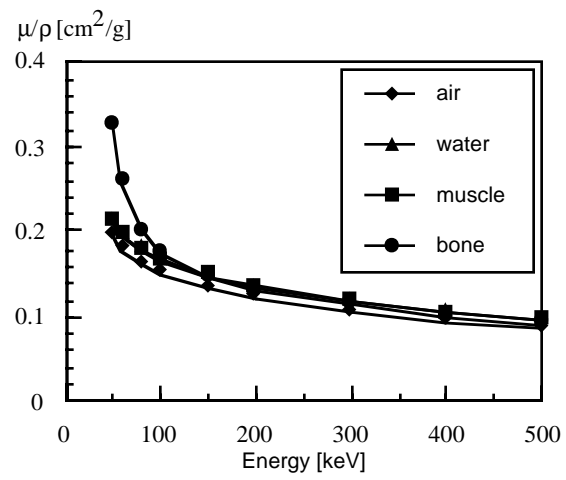
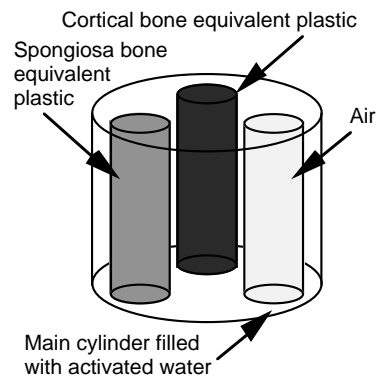
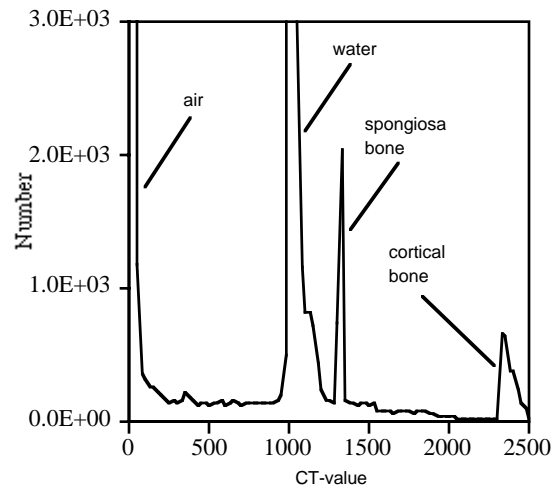


Figure 3



**Figure 4**



**Figure 5**

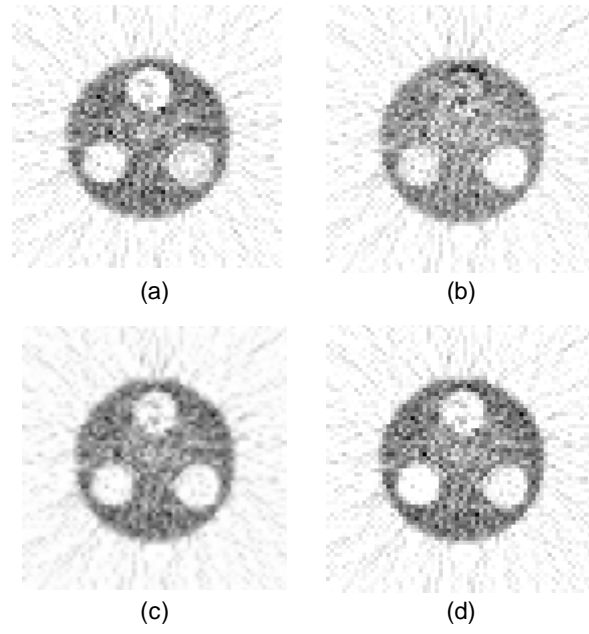


**Figure 6**

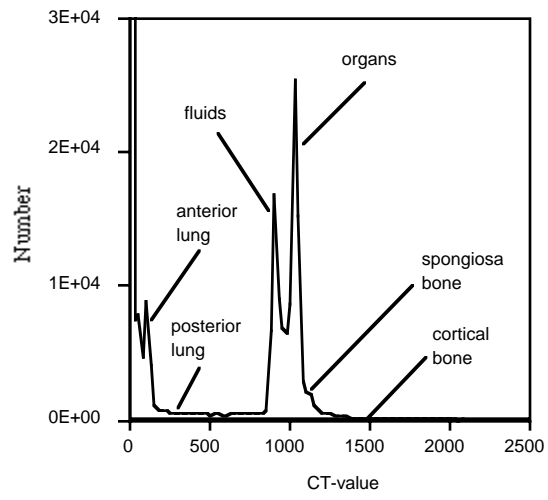


**Figure 7**

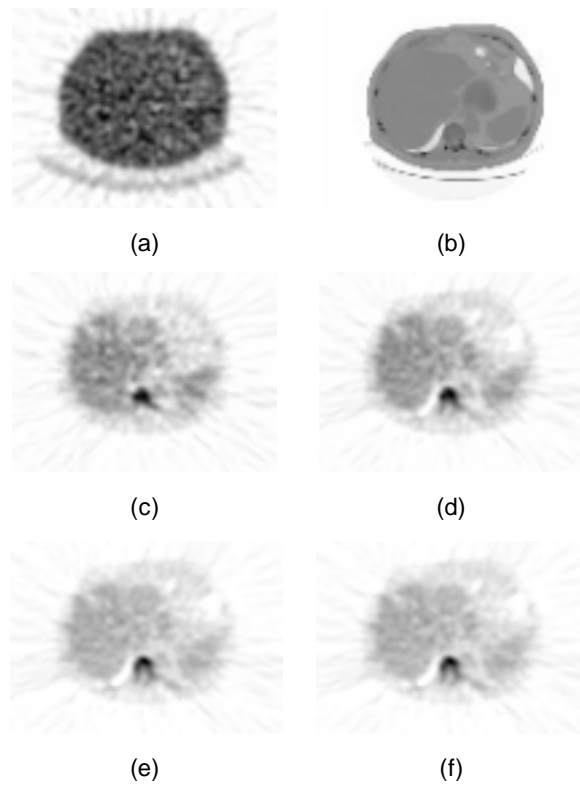


**Figure 8**